GEOPHYSICAL RESEARCH LETTERS, VOL. 34, L19603, doi:10.1029/2007GL031242, 2007

Measurements of the viscous tangential stress in the airflow above wind waves

F. Veron,[1] G. Saxena,[1] and S. K. Misra[1]

Received 5 July 2007; accepted 13 September 2007; published 13 October 2007.

[1] The stress and drag at the surface of the ocean are crucial parameters for both short term forecasting and the modeling of long-term global climate trends. However, the partition between viscous, turbulent, and wave stresses, and in particular the effects of airflow separation are not well understood. We present direct measurements of the velocity in the airflow above wind-generated waves. We observe intermittent separation of the viscous sublayer past the crest of the wind waves leading to dramatic along-wave variability in the surface viscous tangential stress. These results hold for wind speeds that would normally be considered low to moderate. These viscous stress measurements in the airflow above the wavy surface, and within the separated region are, to the best of the authors' knowledge, the first of this kind. **Citation:** Veron, F., G. Saxena, and S. K. Misra (2007), Measurements of the viscous tangential stress in the airflow above wind waves, *Geophys. Res. Lett.*, *34*, L19603, doi:10.1029/2007GL031242.

1. Introduction

[2] The coupled air-sea boundary layers play an important role in the fluxes of momentum, heat, and mass between the atmosphere and the ocean. These exchanges are crucial to the weather and climate, providing important boundary conditions for both the atmosphere and the oceans. The complex dynamics of this coupled system has, in recent years, received considerable attention, in particular in the context of modeling the flow of both fluids in order to improve climate models and predictions.

[3] Our current understanding of the momentum boundary layers on both sides of the air-sea interface is derived from the well-known "law of the wall", which as its name indicates, models the mean turbulent boundary layer flow over flat rigid surfaces. It relies on the assumption that the total stress (sum of viscous and turbulent stresses) is constant in the boundary layer. This leads to the classical self-similar log-linear velocity profile. Over the ocean however, the presence of deformable, moving, surface waves influences the structure and dynamics of the atmospheric boundary layer [e.g., *Janssen*, 1989, 1999; *Belcher and Hunt*, 1993; *Komen et al.*, 1994; *Hare et al.*, 1997; *Edson and Fairall*, 1998]. In fact, within the constant stress layer, over the ocean, a fraction of the stress is carried by the waves and the air-sea momentum flux is instead expressed as the sum of turbulent, wave-coherent, and viscous contributions:

$$\tau = \rho_a u_*^2 = \tau_t + \tau_w + \tau_v = \rho_a \overline{u'w'} + \rho_a \overline{\tilde{u}\tilde{w}} + \mu_a \frac{\partial \overline{u}}{\partial z}. \quad (1)$$

The primes indicate turbulent quantities, the tildes are wave coherent quantities, and the overbars represent ensemble averages. The friction velocity in the air is denoted by u_*, ρ_a is the density of air, and μ_a is the dynamic viscosity. Recent measurements and models of the sea surface drag on the atmosphere at moderate to high wind speeds suggest that most of the surface stress is supported by the wave-coherent stress. In addition, it appears that it is the small gravity-capillary wind waves that carry the bulk of this wave stress, which may be further resolved into a component that leads to wave growth and another associated with flow separation over the waves. There is currently a large interest in the airflow separation over these waves as it is thought to greatly influence the drag at hurricane-type wind-speeds [*Kudryavtsev and Makin*, 2001; *Powell et al.*, 2003; *Donelan et al.*, 2004].

[4] Yet, among all the terms in the air-sea momentum flux partition equation above, the fraction of the wave stress τ_w arising from the airflow separation is arguably the least understood. This is in part due to the difficulty of making measurements within one wave height of the mean water level. To date there are few studies of airflow patterns and separation over water waves [e.g., *Chang et al.*, 1971; *Banner and Melville*, 1976; *Kawai*, 1981, 1982; *Csanady*, 1985; *Weissmann*, 1986; *Kawamura and Toba*, 1988; *Banner*, 1990; *Reul et al.*, 1999; *Kudryavtsev and Makin*, 2001], and two-dimensional velocity measurements showing the separation of the airflow above the surface waves are limited, to our knowledge, to the work of *Kawai* [1982] and *Reul et al.* [1999]. *Kawai* [1982] performed low-resolution velocity measurements but stress estimates from his data were not possible. *Reul et al.* [1999] did not look at wind generated waves in an equilibrium condition, their experiments were performed with mechanically generated waves that were ruffled by the wind, therefore more representative of strongly forced conditions. They carried out stress measurements at 1 to 1.5 cm from the surface, outside of the viscous layer.

[5] In this paper we present experimental evidence of airflow separation over small (albeit at the peak of the spectrum) wind-generated waves. Moreover we present quantitative measurements of the flow field above the wavy surface and within the viscous sublayer leading to a direct measure of the viscous stress. As the flow separates from

[1]College of Marine and Earth Studies, University of Delaware, Newark, Delaware, USA.

0094-8276/07/2007GL031242$05.00

the surface we observe abrupt and large changes in near surface velocity, vorticity, and viscous tangential stress.

2. Experimental Setup

[6] The experiments described here were conducted in the large wind-wave-current tank at the Air-Sea Interaction Laboratory of the University of Delaware. The tank's overall working section is 37 m long. It is 1 m wide and 1.25 m high. Water depth was kept at 0.71 m. The tank is equipped with a programmable, computer controlled, recirculating wind tunnel which generated 10-m equivalent wind speeds of 5.7, 9.5, 12.5 and 14.9 ms^{-1}. The test section was placed at a fetch of 21.1 m. High resolution, two-dimensional velocity fields in the airflow above the surface were collected using a Particle Image Velcocimetry (PIV) system consisting of a digital camera (Dantec Flowsense2M - 1186 $\times$ 1600 pixels) fitted with a 60 mm telephoto zoom lens, and a pulsed Nd-Yag laser (120 mj/pulse, 3–5 ns pulse duration, 50 μs pulse interval.) The camera was placed outside the glass sidewalls of the tank. The dimensions of the field of view captured by the camera were 9.1 cm (vertical) $\times$ 12.3 cm (horizontal-along tank) yielding a pixel resolution of 77 μm. The laser light sheet was approximately 1 mm thick and directed vertically towards the water surface. Finally, the airflow was seeded with 8–12 μm water droplets generated by a commercial fog generator (Microcool Inc.) equipped with 28 fog nozzles which were affixed to the airflow straightener at the location of zero fetch.

[7] For each acquisition run, the wind was slowly increased to its target steady value. After the wave field had sufficiently developed and reached a fetch-limited equilibrium state, the fog generator was started and the system acquired a data set of 256 image pairs over 50.6 s. The fog generator was then stopped in order to avoid significant cooling and water vapor loading of the air. This procedure was repeated until at least 3 data sets were acquired yielding 768 velocity fields for each wind speed. Additional wind speed and wave height data were collected with a pitot tube and a capacitance wire wave gauge, respectively.

[8] The PIV images were processed using the adaptive PIV algorithm described by *Thomas et al.* [2005]. The calculation was run only on the portion of the image above the instantaneous water surface. In order to achieve this, the air-water interface within each image was detected automatically [*Misra et al.*, 2005]. The estimated surface profiles were checked visually for validity and accuracy. The surface location was subsequently used to project the variables of interest from the image-attached Cartesian coordinate system (x, z) to a local, surface-following, curvilinear coordinate system (t, n) where t and n are unit vectors locally tangent and normal to the surface respectively.

3. Results

[9] We show here an example of a single velocity field which shows the separation of the viscous boundary layer above the wind-generated waves. This velocity field was chosen among the faction of PIV realizations that exhibit a separation event. It should be stressed however that the results shown here are not a "best pick" and are typical and representative of the available data.

3.1. Velocity in the Airflow

[10] Figure 1a shows a composite vector plot of air velocity for a typical airflow separation event. The results have been plotted over the waterside portion of the original digital image (that was excluded from the PIV calculation). This image is a composite data image generated by merging two independent PIV fields separated by 0.19 s. The merging position (shown by double vertical arrow) was estimated using the wave phase speed calculated from the wave gauge data. The surface profile and data are continuous indicating that there is little change in the overall structure of the airflow in this short time interval. The vector plot, for clarity, only shows a fifth of the available data in each direction. Figure 1a shows that the airflow is attached to the wave on the windward side where the viscous sublayer is very thin (barely visible in the velocity field). On the leeward side of the wave, there is a large turbulent region, presumably generated by the boundary layer separation. Some large coherent vortices are clearly visible in Figure 1a. The turbulent cloud disappears around $\frac{X}{\lambda} \approx 0.5$–0.6, where X is the along wind distance from the wave crest and λ the wavelength. It should be noted that the data shown here are taken from a single detachment event and that the turbulent nature of the flow makes it impossible to identify a single, clear, and well defined reattachment point as some readers might expect from phase averaged data or schematics. Here, the reattachment is instead evident from the thinning of the turbulent cloud past the trough of the wave and the re-establishment of the viscous sublayer. This is perhaps better shown on Figure 1b, which shows the wind speed magnitude. The detached region exhibits low velocity, as it is dominated by turbulence where the air velocity is significantly lower than the free stream velocity above the wave crest.

[11] We then evaluate near-surface values of the air velocity and present three different estimates. U_s is calculated from the surface value (or closest estimate at an average height z_s = 154 μm from the surface) of the tangential component of the air velocity $U_t(z)$:

$$U_s = U_t(z_s). \tag{2}$$

We also calculate U_v and U_b which are the averaged values of $U_t(z)$, up to the height of the viscous and buffer regions, respectively. Accordingly,

$$U_v = \frac{1}{z|_{z^+=12}} \int_0^{z^+=12} U_t(z)dz, \tag{3}$$

and

$$U_b = \frac{1}{z|_{z^+=30}} \int_0^{z^+=30} U_t(z)dz. \tag{4}$$

Here, $z^+ = \frac{zu_*}{\nu_a}$ is the so-called wall layer coordinate which depends solely on the friction velocity u_*, the air viscosity ν_a, and the height from the surface z. Figure 1c shows these near-surface velocities for the data shown on Figures 1a and 1b. The near-surface velocities are calculated

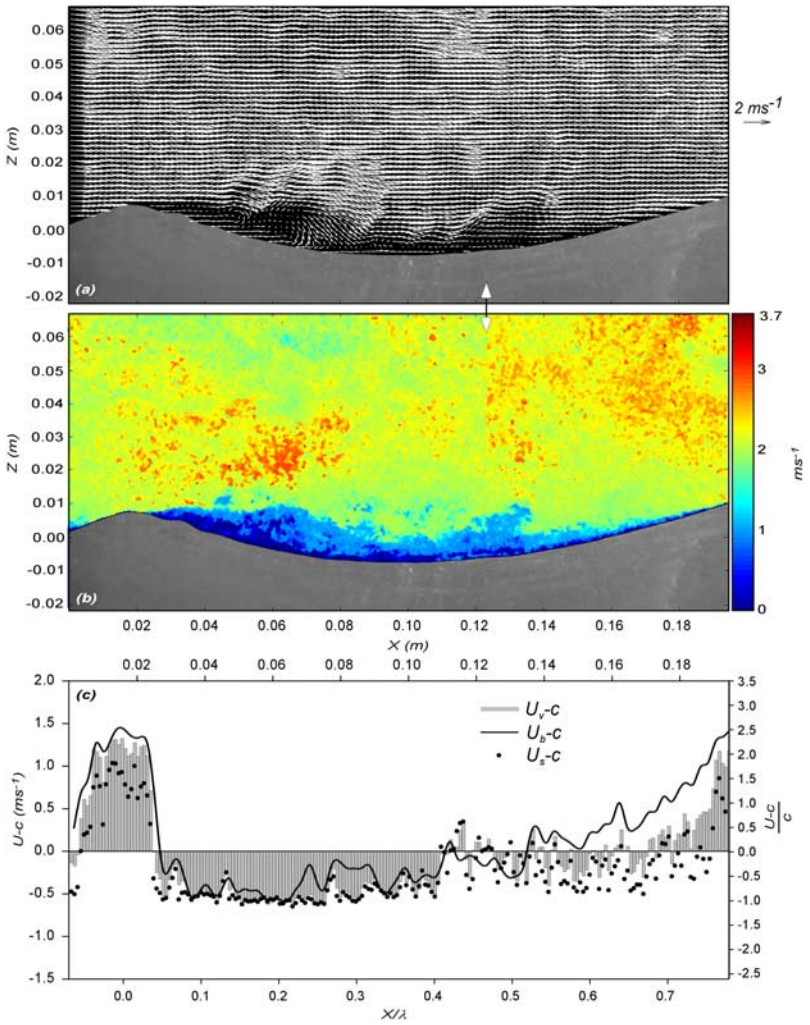

Figure 1. (a) Velocity vector plot of the separating airflow over the waves for a wind speed of $U_{10} = 5.7$ ms^{-1}. (b) Velocity magnitude in the airflow. (c) Near surface estimates of the velocity tangential to the surface U_s, U_v and U_b. The velocities are shown in a frame of reference moving with the surface wave with a phase speed c. The right hand side scale shows these relative velocities scaled by the wave phase speed.

in a frame of reference moving with the surface wave and bin averaged along surface direction t, over a distance of $z^+ = 12$. The data show that the surface velocity U_s is highest on the windward face of the wave with its peak value at the wave crest. In this region, U_s is lower than the viscous surface velocity U_v which is in turn lower than the buffer velocity U_b. This is to be expected from the classical log-linear turbulent velocity profile. All estimates show that the air is moving faster than the waves. Past the crest, the estimates of the near-surface velocity abruptly drop and become negative, indicating that the air, relative to the wave, is moving toward the crest. All estimates also collapse to the same value indicating that the classical log-linear velocity profile is lost and that the profile is roughly uniform, at least up to heights as large as the buffer region. Past the trough of the wave, the near-surface velocities gradually become positive again and re-order with $U_s \leq U_v \leq U_b$ indicating the gradual re-generation of the viscous and buffer layers.

3.2. Vorticity and Viscous Stresses

[12] Figure 2a shows the instantaneous streamline pattern for the same data. It shows that before the crest, the streamlines are relatively organized and parallel, all the way down to the surface. As the flow approaches the crest, the streamlines start compressing and contracting. As the flow passes the wave crest, the streamlines diverge and the along surface flow starts decelerating. In this case, the flow near the surface reverses and starts moving toward the wave crest. The streamlines appear to reconnect to the surface at $\frac{X}{\lambda} \approx 0.5-0.6$, the region where the viscous sublayer starts re-establishing.

[13] While the streamlines and velocity fields (and in particular within the viscous layer) presented above suggest that the airflow is indeed separating, this is better established by examining Galilean invariant fields such as the vorticity. Figure 2b shows the instantaneous vorticity field corresponding to the data of Figure 1a. On the windward side of the wave, there is a thin region of very high vorticity (dominated by shear), attached to the surface, which is the signature of the viscous sublayer. As the flow separates, the vortical/shear layer leaves the surface. This vortical/shear layer remains coherent and clearly visible in Figure 2b for some distance. In fact, the turbulent detached region and the

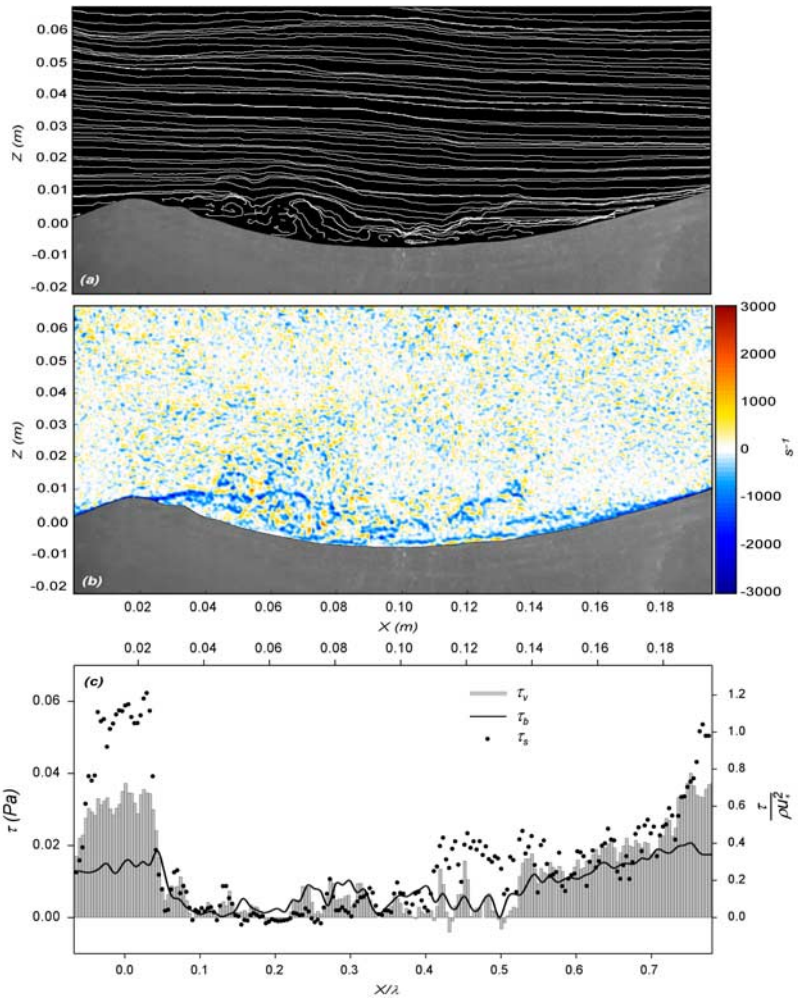

Figure 2. (a) Instantaneous streamline pattern for the data of Figure 1. (b) The corresponding vorticity field and (c) the viscous tangential stress closest to the surface $\tau_s = \mu_a \frac{\partial U_s}{\partial n}$, along with τ_v and τ_b. The right hand side scales shows these stresses scaled by the total stress $\rho_a u_*^2$.

remaining undisturbed flow above are relatively well segregated by this shear layer. This is also visible in Figure 2a where one can clearly identify a streamline that separates the mean flow above the wave crest and the detached turbulent region. The high shear in the flow, unsupported by the surface, is unstable and the vortical thin layer, breaks down, mixes, and disappears. We note here that this vortical layer sometimes exhibits vertical oscillations that are reminiscent of classic shear instabilities with large coherent vortices. The airflow separation acts as a source of vorticity in the flow and therefore enhances mixing in the separated region. As the flow gradually reattaches on the leeward side of the next wave, the vortical layer attached to the surface gradually reforms.

[14] Figure 2c shows the near-surface viscous tangential stresses along the surface. The behavior of the near surface stresses is consistent with that of the near surface velocity (see below). The data show that the surface tangential stress τ_s is highest on the windward face of the wave with its peak value at the wave crest. In this region, τ_s is significantly higher than both the stresses averaged through the viscous sublayer τ_v and that averaged through the buffer region τ_b Again, this is to be expected and is a consequence of the high shear in the viscous sublayer, and the rapid spatial variation of the stress in this region. It should be noted here that the closest stress measurement available (z = 154 μm) already indicates that, at least locally, at the wave crest, the viscous tangential stress is perhaps more than the total average stress ρu_*^2. Values on the surface at z = 0 are expected to be even higher. Once the flow detaches, all estimates of the near-surface viscous stresses abruptly drop and collapse to approximately 0, indicating once again the loss of coherent shear and velocity profiles at heights up to the buffer region. Past the trough of the wave, the near-surface stresses gradually become positive again and re-orders with $\tau_b \leq \tau_v \leq \tau_s$ indicating the gradual re-generation of the viscous and buffer layers.

[15] The figures shown above are taken for a wind speed of U_{10} = 5.7 ms^{-1}. We note here that these data are quite typical and that there are no significant qualitative differences in the data taken for wind speeds ranging from 4.5 ms^{-1} to 14.9 ms^{-1}.

4. Discussion

[16] We have successfully measured the near surface velocity and viscous tangential stress at a distance of approximately 154 μm from the surface (within the viscous

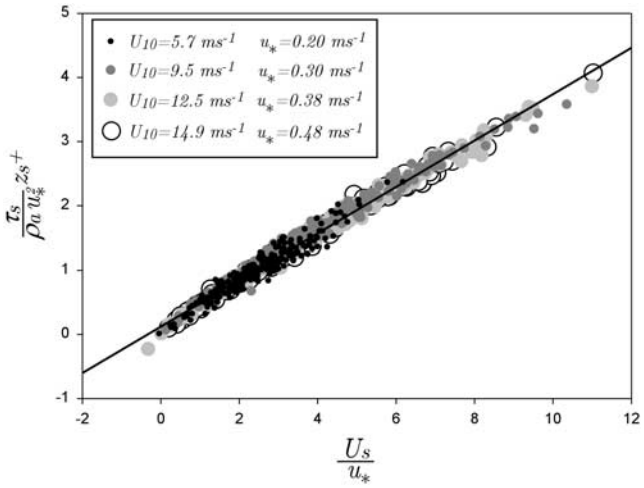

Figure 3. Non-dimensional surface stress as a function of the non-dimensional surface velocity for all wind speeds.

sublayer) and also averaged over the viscous and buffer layers. Our data show clear evidence of airflow separation over small wind-generated waves. We have shown that airflow separation leads to a dramatic reduction of the near surface velocity, with a sign reversal, indicating the presence of what is usually referred to as a recirculating bubble. Concurrently, the viscous tangential stress near the surface dramatically drops at the point of separation leading to extreme along-wave variability of order $\rho_a u_*^2$ in the span of half a wavelength.

[17] The similarity in behavior of the surface stress and velocity led us to examine possible functional link between the two. Figure 3 shows a plot of the surface stress τ_s as a function of the surface velocity U_s. Here, the stress and velocity are averaged for each data image yielding 256 estimates per wind speed. The surface velocity is normalized by the friction velocity and the stress by the total turbulent stress, multiplied by the non-dimensional (wall coordinate) height of the surface estimate z_s. Figure 3 shows that the data collapse for all wind speeds and are consistent whether or not the flow detaches. The collapse is quite robust (r^2 = 0.98) and independent of wind conditions.

[18] The common occurrence of airflow separation at low to moderate wind speeds suggest that the linear and non-separated wave generation and growth models [e.g., *Miles*, 1957, 1962; *Valenzuela*, 1976; *Kawai*, 1979; *Wheless and Csanady*, 1993; *Belcher*, 1999] might be inadequate in all but the very initial stages of the wave generation process, and in very low wind speed conditions. Yet, correlations between surface stress and surface velocity indicate that simple measurements or models of the surface velocity fields might be adequate avenues to determining the usually more elusive surface stress parameters.

[19] **Acknowledgments.** We wish to thank Emily Harrison and Luc Lenain for their help with the experimental procedures and James Mueller for his detailed review of the paper. We also thank Mike Banner and Ken Melville for numerous fruitful discussions.

References

Banner, M. L. (1990), The influence of wave breaking on the surface pressure distribution in wind wave interaction, *J. Fluid Mech.*, *211*, 463–495.

Banner, M. L., and W. K. Melville (1976), On the separation of airflow over water waves, *J. Fluid Mech.*, *77*, 825–842.

Belcher, S. E. (1999), Wave growth by non-separated sheltering, *Eur. J. Mech. B*, *3*, 447–462.

Belcher, S. E., and J. C. R. Hunt (1993), Turbulent shear flow over slowly moving waves, *J. Fluid Mech.*, *251*, 119–148.

Chang, K., E. J. Plate, and G. M. Hidy (1971), Turbulent air flow over the dominant compononet of wind-generated water waves, *J. Phys. Oceanogr.*, *15*, 1486–1501.

Csanady, G. T. (1985), Air-sea momentum transfer by means of short-crested wavelets, *J. Fluid Mech.*, *47*, 183–208.

Donelan, M. A., B. K. Haus, N. Reul, W. J. Plant, M. Stiassnie, H. C. Graber, O. B. Brown, and E. S. Saltzman (2004), On the limiting aerodynamic roughness of the ocean in very strong winds, *Geophys. Res. Lett.*, *31*, L18306, doi:10.1029/2004GL019460.

Edson, J. B., and C. W. Fairall (1998), Similarity relationships in the marine surface layer, *J. Atmos. Sci.*, *55*, 2311–2328.

Hare, J. E., T. Hara, J. B. Edson, and J. M. Wilczak (1997), A similarity analysis of the structure of airflow over surface waves, *J. Phys. Oceanogr.*, *27*, 1018–1037.

Janssen, P. A. E. M. (1989), Wind induced stress and the drag of air flow over sea waves, *J. Phys. Oceanogr.*, *19*, 745–754.

Janssen, P. A. E. M. (1999), On the effect of ocean waves on the kinetic energy balance and consequences for the inertial dissipation technique, *J. Phys. Oceanogr.*, *29*, 530–534.

Kawai, S. (1979), Generation of initial wavelets by instability of a coupled shear flow and their evolution to wind waves, *J. Fluid Mech.*, *93*, 661–703.

Kawai, S. (1981), Visualization of airflow separation over wind-wave crests under moderate wind, *Boundary Layer Meteorol.*, *21*, 93–104.

Kawai, S. (1982), Structure of airflow separation over wind wave crests, *Boundary Layer Meteorol.*, *23*, 503–521.

Kawamura, H., and Y. Toba (1988), Ordered motion in turbulent boundary layer over wind waves, *J. Fluid Mech.*, *197*, 105–138.

Komen, G. J., M. Cavaleri, M. Donelan, K. Hasselmann, S. Hasselmann, and P. Janssen (1994), *Dynamics and Modeling of Ocean Waves*, Cambridge Univ. Press, Cambridge, U. K.

Kudryavtsev, V. N., and V. K. Makin (2001), The impact of air-flow separation on the drag of the sea-surface, *Boundary Layer Meteorol.*, *98*, 155–171.

Miles, J. W. (1957), On the generation of surface waves by shear flow, part I, *J. Fluid Mech.*, *3*, 185–204.

Miles, J. W. (1962), On the generation of surface waves by shear flow, part IV, *J. Fluid Mech.*, *13*, 433–448.

Misra, S. K., M. Thomas, C. Kambhamuttu, J. T. Kirby, F. Veron, and M. Brocchini (2005), Estimation of complex air water interface from PIV images, *Exp. Fluids*, *40*, 764–775.

Powell, M. D., P. J. Vickery, and T. A. Reinhold (2003), Reduced drag coefficient for high wind speeds in tropical cyclones, *Nature*, *422*, 279–283.

Reul, N., H. Branger, and J. P. Giovanangeli (1999), Air-flow separation over unsteady breaking waves, *Phys. Fluids*, *87*, 1961–1967.

Thomas, M., S. K. Misra, C. Kambhamettu, and J. T. Kirby (2005), A robust motion estimation algoritm for PIV, *Meas. Sci. Technol.*, *16*, 865–877.

Valenzuela, G. R. (1976), The growth of gravity-capillary waves in a coupled shear flow, *J. Fluid Mech.*, *76*, 229–250.

Weissmann, M. A. (1986), Observations and measurements of air flow over water waves, in *Wave Dynamics and Radio Probing of the Sea Surface*, edited by O. M. Phillips and K. Hasselmann, pp. 335–352, Plenum, New York.

Wheless, G. H., and G. T. Csanady (1993), Instability waves on the air-sea interface, *J. Fluid Mech.*, *248*, 363–381.

S. K. Misra, G. Saxena, and F. Veron, College of Marine and Earth Studies, University of Delaware, 112C Robinson Hall, Newark, DE 19716, USA. (fveron@udel.edu)